# Mechanical properties and structural stability of a bulk nanostructured metastable aluminum-magnesium system

Jae-Kyung Han [a], Klaus-Dieter Liss [b,c,d], Terence G. Langdon [e], Jae-il Jang [f], Megumi Kawasaki [a,*]

[a] School of Mechanical, Industrial and Manufacturing Engineering, Oregon State University, Corvallis, OR, 97331, USA
[b] Materials and Engineering Science Program, Guangdong Technion - Israel Institute of Technology, Shantou, Guangdong, 515063, China
[c] Technion – Israel Institute of Technology, Haifa, 32000, Israel
[d] School of Mechanical, Materials, Mechatronic and Biomedical Engineering, University of Wollongong, Wollongong, NSW, 2522, Australia
[e] Materials Research Group, Department of Mechanical Engineering, University of Southampton, Southampton, SO17 1BJ, UK
[f] Division of Materials Science and Engineering, Hanyang University, Seoul, 04763, Republic of Korea

ABSTRACT

The mechanical properties and structural stability of a high-pressure torsion (HPT)-induced bulk nanostructured metastable Al–Mg system were examined after natural aging at room temperature for 60 days. The sample demonstrated a high yield strength of 1.3–1.5 GPa with an excellent plasticity by achieving a high strain rate sensitivity of 0.036. The high hardness is attributed to the concurrent contributions of grain refinement and solid solution strengthening. An X-ray diffraction analysis revealed a high compositional microstrain of ~0.0202 due to the supersaturation of Mg in the Al matrix after processing. This microstrain increased to ~0.0274 after natural aging due to the heterogeneous distribution of supersaturated Mg solutes without any nucleation of a second phase, thereby demonstrating a reasonable structural stability.

## 1. Introduction

The formation of bulk nanostructured materials has been studied intensively in the last two decades together with the development of severe plastic deformation (SPD) processing techniques [1–3]. Among the available SPD techniques, one of the most attractive methods is high-pressure torsion (HPT) [4] where often the process is operational at room temperature for most hard-to-deform metals and composites and significant grain refinement may be anticipated by comparison with other SPD procedures [5]. Accordingly, processing by HPT has been utilized for the bonding of machining chips [6–8] and the consolidation of metallic powders [9–15] which may ultimately produce intermetallics and supersaturation phases leading to composites [16,17].

Considering these benefits of HPT processing, a new approach into the mechanical-bonding processes was developed for the synthesis of hybrid nanostructured metallic materials where this approach applies the conventional HPT technique for diffusion bonding of dissimilar bulk metal disks. Various combinations of dissimilar metals were examined to date: Al/Cu [18–23], Al/Mg [24–32], Al/Fe [33], Al/Ni [22], Al/Ti [33], Al/Mg/Cu/Fe/Ti [34], Ag/Cu [20], Ag/Ni [35], Cu/Ta [36,37], Cu/ZnO [38], Fe/V [39,40], V–10Ti–5Cr/Zr-2.5Nb [41], Zn/Mg

[42–44] and Zr/Nb [35,45]. These studies demonstrated the successful synthesis of intermetallic phases during HPT-induced diffusion bonding at room temperature.

The experiments showed that these metastable phases including intermetallic compounds are nucleated at the vicinity of the interfaces of dissimilar metals when severe shear is introduced by the HPT-induced mechanical bonding and the mechanism can be understood through the formation of tribomaterials [46]. In practice, there are unique flow patterns, similar to the flow of liquids, that appear as vortices adjacent to the interfaces when a Kelvin-Helmholtz (K–H) shear instability [47,48] occurs under shear or sliding deformation. These K–H instabilities were documented in an earlier report on HPT processing [49] and they are consistent with observations from many areas of physics including in fluid flow [50], plasma physics [51], atmospheric physics [52] and oceanography [53]. Recent reports demonstrated a physical explanation of the microstructural patterns at the dissimilar solid interfaces during plastic flow that is driven by plastic instabilities due to local blocking of shear deformation [22,54,55]. Thus, the interfaces in the mechanically-bonded metals undergo severe shear at high pressure by HPT and this introduces, through plastic instability, large volumes of nanocrystalline tribomaterials during the phase mixture and grain

---

refinement.

As one of the ultimate states during the introduction of an Al–Mg tribomaterial, a very recent study showed the formation of a bulk nanostructured metastable Al solid solution with a homogeneous supersaturation of Mg when Al and Mg are mechanically bonded through 100 HPT turns at 6.0 GPa [32]. Accordingly, the present study was initiated to examine the mechanical response and structural stability of the HPT-induced bulk nanostructured metastable Al–Mg alloy by applying nanoindentation and an X-ray diffraction (XRD) peak profile analysis.

## 2. Experimental material and procedures

A bulk nanocrystalline metastable Al–Mg was prepared by mechanical bonding of a commercial purity Al (Al-1050) and a ZK60 Mg alloy by stacking the metal disks having 10 mm diameter and 0.8 mm thickness in the order of Al/Mg/Al and processing through HPT for 100 turns at 6.0 GPa at room temperature. The synthesized metastable alloy was maintained at room temperature for natural aging for 60 days to investigate the structural stability. In an earlier study, this metastable Al solid solution showed an average Mg content of ~14 at.% with a maximum of 38.44 at.% and an ultrafine-grained microstructure having ~35–40 nm grains in a fully metastable state without any trace of h.c.p. Mg or intermetallic phases for both conditions of 100 HPT turns and after HPT and natural aging for 60 days [32].

Vickers microhardness measurements were conducted to construct hardness profiles along the diameters on the mid-sectional planes of the mechanically-bonded Al–Mg disks after HPT. The Vickers microhardness values, Hv, were recorded using a Mitutoyo HM-200 with an applied load of 50 gf and a dwell time of 10 s.

The detailed mechanical responses were examined using a nanoindentation facility, Nanoindenter G200 XP, at the mid-radius of naturally-aged metastable Al–Mg disks. To validate the data, more than 15 indentations were conducted for the HPT-processed metastable Al–Mg after natural-aging. All measurements were undertaken using a predetermined maximum applied load of $P_{max}$ = 50 mN at constant indentation strain rates of 0.0125, 0.025, 0.05 and 0.1 s$^{-1}$ which are equivalent to general strain rates, $\dot{\varepsilon}$, of $1.25 \times 10^{-4}$, $2.5 \times 10^{-4}$, $5.0 \times 10^{-4}$ and $1.0 \times 10^{-3}$ s$^{-1}$, respectively, according to an empirical relationship [56].

The X-ray diffraction (XRD) analyses were performed using a Rigaku Ultima III over the entire disk surfaces to acquire overall structural information of the mechanically-bonded and naturally-aged materials. The XRD facility used Cu K$\alpha$ radiation at a scanning speed of 1° min$^{-1}$ with a step interval of 0.01°. Further analyses were conducted by the XRD line profiles in order to identify the structural changes and quantifying microstrains.

## 3. Experimental results

### 3.1. Mechanical response of metastable Al–Mg alloy

From the Vickers microhardness measurements, a homogeneous distribution of hardness with an average hardness of Hv ≈ 340 was recorded across the Al–Mg disk diameter after 100 HPT turns [32]. Such extreme and homogeneous hardness across the disk diameter is in contrast to the mechanically-bonded Al–Mg disks after HPT for up to 60 turns [28,29]. These hardness results are summarized in Fig. 1 where the two lower dashed lines denote the saturated hardness values of the separate Al and Mg alloys when processed for 5 or more HPT turns at 6.0 GPa.

The micro-mechanical responses of the metastable Al–Mg alloy after HPT followed by aging were examined using a nanoindentation technique and the results are compared with the alloy system processed by mechanical bonding of the Al–Mg sample after 40, 60 and 80 HPT turns. An evaluation of micro-mechanical responses considers the evolution of
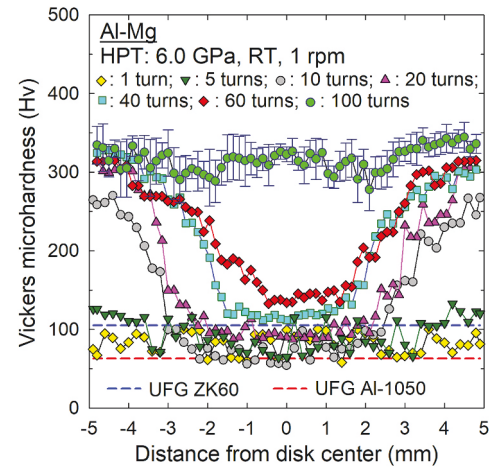


**Fig. 1.** Hardness values of an HPT-induced Al–Mg system after HPT for 1 to 100 turns including the hardness values reported earlier for up to 60 turns [28, 29] under 6.0 GPa at room temperature.

the strain rate sensitivity, $m$, as a critical materials property which is generally determined by

$$m = \left(\partial \ln \sigma_f / \partial \ln \dot{\varepsilon}\right)_{\varepsilon,T} \tag{1}$$

where $\sigma_f$ is the uniaxial flow stress and $\dot{\varepsilon}$ is the strain rate where these parameters are related at a given strain, $\varepsilon$, and temperature, $T$ [57]. Moreover, $\sigma_f$ can be estimated by Tabor's empirical relation of $\sigma_f \approx H/C$ where $C$ is a constrain factor of ~3 for fully plastic deformation at the constant nanoindentation strain rates [58] and $H$ is the nanoindentation hardness. Thus, the value of $m$ is estimated from the slope of a double logarithmic plot of $H/3$ vs. $\dot{\varepsilon}$ as shown in the inset of Fig. 2. From the positions of the lines, it is apparent that the Al–Mg system after 100 HPT turns demonstrated the highest strength of $\sigma_f$ = 1.3–1.5 GPa at the examined strain rates. There is also a clear trend of increasing $m$ values with increasing HPT turns after 40 turns and the maximum value was computed as $m$ = 0.036 for the bulk metastable Al–Mg after 100 turns.

The evolution of $m$ with increasing HPT revolutions through 5–100 turns is shown for the Al–Mg samples in the main part of Fig. 2. A low strain rate sensitivity of <0.01 and close to a negative value was recorded when mechanical bonding of Al and Mg was conducted through the lower numbers of HPT turns of 5 and 20, respectively, and this is due to the introduction of hard intermetallic phases of $Al_2Mg_3$ and $Al_{12}Mg_{17}$ through diffusion bonding during microstructural refinement
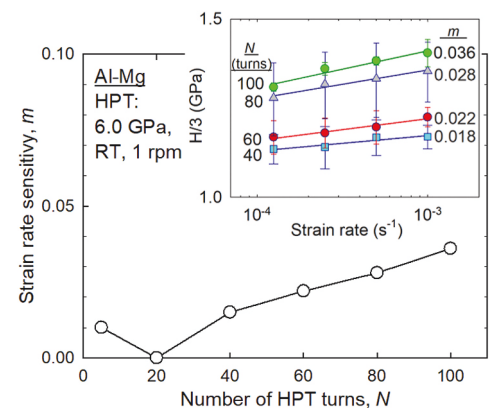


**Fig. 2.** Variation in strain rate sensitivity with different levels of torsional straining for the mechanically-bonded Al–Mg. (an inset shows the value of $m$ estimated from the slope of the double logarithmic plot of $H/3$ vs. $\dot{\varepsilon}$ for the samples after HPT for 40–100 turns).

by HPT leading to the formation of metal matrix nanocomposites [26–28]. Thereafter, the estimated $m$ values increase with increasing HPT turns through 100 turns. This is reasonable because of the formation of a single solid solution phase of Al having an *f.c.c.* Crystal structure by the complete dissolution of these intermetallic phases only at the disk edges after 40 and 60 HPT turns while the disk centers demonstrate multi-layers of Al and Mg [29] and thereafter through the entire metastable body of the Al–Mg disk after 100 turns followed by natural aging [32].

In general, a high value of $m$ corresponds to a high capacity to produce improved plasticity of the material and therefore the trend shown in Fig. 2 implies exceptional increases in both strength and plasticity in the HPT-induced bulk metastable Al–Mg after 100 HPT turns under the present testing conditions. It should be noted that these values of $m$ after HPT are similar to or even higher than the values for UFG Al alloys (e.g., $m \approx 0.02$ for Al-1570 after 20 HPT turns having a grain size of $d < 100$ nm [59]), UFG Mg alloys (e.g., $m \approx 0.035$–0.045 for ZK60 after 2 HPT turns having $d < 1.0$–1.5 μm [60]), and various UFG metals and alloys after different types of SPD processing [61]. Thus, the present bulk metastable Al–Mg exhibits reasonably high plasticity while demonstrating extreme $\sigma_f$ and hardness.

### 3.2. X-ray line broadening

Earlier compositional analysis using STEM investigations confirmed an Mg supersaturated concentration leading to a metastable Al alloy after HPT for 100 turns where the highest recorded dissolved quantity of Mg was ~38.5 at.% [32]. In order to determine whether such high Mg supersaturation occurs homogeneously rather than locally, and to examine the stability of the structure after 60 days of natural aging, the Mg concentration in the metastable Al solid was examined by utilizing the XRD line profiles taken integrally over the whole sample surface plane.

Fig. 3 shows the distributions of the lattice parameters estimated from the four separate XRD peaks for a pure *f.c.c.* structure, such as 111, 200, 220 and 331, with an arbitrarily selected counting probability for the metastable Al alloy immediately after HPT (upper) and after natural aging (lower) where the vertical dashed line in each plot denotes the lattice parameter for pure Al of $a_0 = 4.049$ Å. Maintaining cubic symmetry, the distributions of the lattice parameter tend to be independent of these four reflections for both sample conditions so that the four separate curves overlap reasonably. Assuming a change in lattice
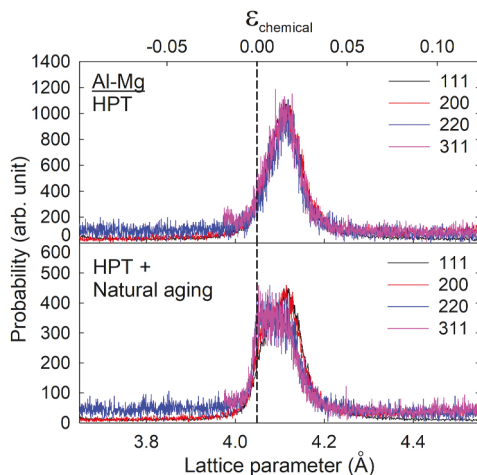


**Fig. 3.** Distributions of lattice parameters (lower transverse axis) and the chemical strain (upper transverse axis) for the four separate XRD reflections for the metastable Al after HPT (upper) and after natural aging (lower), respectively; a vertical dashed line denotes the lattice parameter of 4.049 Å for pure Al in each plot.

parameter of the metastable Al solid solution because of the strain caused solely by the lattice strain effects, the top abscissa measures the lattice deviation from pure Al in the total strain by $\varepsilon_{chemical} = \Delta a/a_0 = -\Delta G/G_0$ for any of the scattering vectors $G_{hkl}$ of the four observed reflections.

It is readily apparent from inspection of Fig. 3 that the plateau behavior in the XRD line profile is strengthened in the plot for the metastable material after natural aging. This particular broadening is attributed mainly to a heterogeneous Mg concentration in many different grains. In practice, for the aged metastable Al alloy the distributions of Mg for the higher order reflections of 220 and 311 tend to shift to a lower Mg concentration as compared to the lower order 111 and 200 reflections. Specifically, this heterogeneous distribution of Mg solute during natural aging can be explained by the clustering and segregation of Mg atoms and ultimately to the decomposition of $Al_3Mg_2$ precipitations at grain boundaries [62] with very specific orientations with respect to the *f.c.c.* Al matrix [63] whereas there is no second phase in the present metastable Al after natural aging for 60 days.

From the viewpoint of the characterization technique, it is important to also consider another explanation for the observed plateau line broadening for the metastable Al after HPT followed by natural aging. The mass absorption coefficients for X-rays at 8 keV are taken for Mg and Al as $\Sigma_{Mg} = 40.61$ cm$^2$/g and $\Sigma_{Al} = 50.33$ cm$^2$/g, respectively, from the NIST Standard Reference Database [64]. The elemental densities of Al and Mg are $\rho_{Al} = 2.700$ g/cm$^3$ and $\rho_{Mg} = 1.738$ g/cm$^3$, respectively [65]. Taking the atomic concentrations of $c_{Mg} = 0.4$ and $c_{Al} = 0.6$ as estimated for the metastable Al–Mg alloy, it is reasonable to estimate the density of the metastable Al as $\rho = c_{Mg} \rho_{Mg} + c_{Al} \rho_{Al} = 2.3152$ g/cm$^3$ and similarly the mass absorption coefficient of $\Sigma = c_{Mg}\Sigma_{Mg} + c_{Al}\Sigma_{Al} = 46.442$ cm$^2$/g. The attenuation length in X-ray scattering, $t$, at which the intensity drops to $1/e$ times its incident flux ($e = \exp(1) = 2.7182818$, Eulerian number) is then given by $t = 1/(\rho\Sigma) = 93.0$ μm. As the four observed Bragg reflections 111, 200, 220 and 311 diffract under their specific incident angles of $\theta = \{19.14, 22.25, 32.38, 38.90\}°$ in a Bragg-Brentano geometry, their beam paths through the metastable Al are different at computed probing depths of $\tau = t/2 \sin(\theta) = \{15, 18, 25, 29\}$ μm, respectively, from the surface of the material. Therefore, a depth gradient of concentration will produce various lattice parameter distributions measured by the different reflections.

The present X-ray diffraction analysis illustrates a unique feature of diffractograms where the aged material demonstrates the inclined plateaus for the low-order reflections 111 and 200 in contrast to the flat plateaus of the higher order observations at 220 and 331. This is attributed not only to the heterogeneous distribution of Mg solutes on the measured surface but also to the heterogeneous compositions which were developed through the thickness of the processed disk during aging. Since the 311 reflection probes the material twice as deeply as the 111 reflection, it is speculated that such a depth-dependent variation exists when the material contains the heterogeneous distributions of alloying elements in the sample height (or thickness) direction. This finding is consistent with a very recent report demonstrating a thickness-resolved order-disorder phase transition in titanium aluminide after HPT for 10 turns [66] and the formation of architectured materials by severe changes of internal structural patterns during SPD [67], and these effects are anticipated due to the heterogeneous deformation produced by the rolling vortices and swirls that are developed through simple shear in HPT processing [20,49,68–71].

A conventional Williamson-Hall plot is shown in Fig. 4 displaying full width at half maximum (FWHM), $\Delta Q$, of the XRD peak profiles against the scattering vector, $Q$, so that the result of microstrain, both compositional and stress-induced, as crystal imperfection and distortion of $\varepsilon = \Delta Q/Q$ may be estimated from the slopes of the fitted straight lines. Thus, the values of ~0.0202 and ~0.0274 for the HPT-induced metastable Al alloy and after natural aging, respectively, repeat the FWHM on the upper strain axes, $\varepsilon_{chemical}$, of Fig. 3 and represent the average lattice strain values due to compositional strain. An earlier report on a
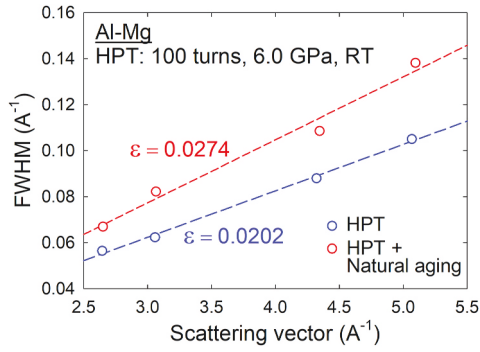
Fig. 4. Williamson-Hall plot for the metastable Al immediately after HPT for 100 turns and the material after natural aging.

nanocrystalline Al-5 at.% Mg alloy prepared by a mechanical alloying approach demonstrated a supersaturation of 4.5 mass% Mg (= 5.0 at.% Mg) in the Al matrix with a lattice strain of 0.0016 [72].

## 4. Discussion

### 4.1. Significance of solution strengthening

In the earlier study, the HPT-induced metastable Al in a solution state barely exhibited deformation twinning [32]. The limited potential of deformation twinning is supported by a study applying generalized planar fault energy calculations [73] computing the maximum twinnability of the Al–Mg dilute solution demonstrating much less than pure Cu. These results are also consistent with an earlier experiment on an Al-5.8 wt.% Mg alloy where there was no deformation twinning in grain sizes of ~100–200 nm but instead there was an agglomeration of Mg atoms observed as clusters of ~5–10 nm at grain boundaries during HPT for up to 20 turns [59].

Accordingly, excluding the contribution of deformation twins to the total strength, the yield strength of the metastable Al, $\sigma_y$, may be estimated as

$$\sigma_y = \sigma_{HP} + \sigma_{SS} \tag{2}$$

where the strength contributed by grain refinement, $\sigma_{HP}$, is defined by the Hall-Petch relationship [74,75]:

$$\sigma_{HP} = \sigma_0 + k_y d^{-1/2} \tag{3}$$

where $\sigma_0$ is the friction stress and $k_y$ is a yielding constant, and the increase in stress due to solid solution strengthening, $\sigma_{SS}$, is obtained from the following equation [76]:

$$\sigma_{SS} = M \left(\frac{3}{8}\right)^{2/3} \left(\frac{1+\nu}{1-\nu}\right)^{4/3} \left(\frac{w}{b}\right) \mu |\varepsilon_m|^{4/3} X_{Mg}^{2/3} \tag{4}$$

where $M$ is the Taylor factor, $\nu$ is Poisson's ratio, $w$ is a material parameter designated the interaction force range, $b$ is the Burgers vector, $\mu$ is the shear modulus, $\varepsilon_m$ is the misfit strain calculated by $(a - a_0)/a_0$ and $X_{Mg}$ is the concentration of Mg. The computation process involves taking $\sigma_0 = 10$ MPa [77] for pure Al, $k_y = 0.2$ [78] for Al–Mg alloys, $M = 3.06$ [79], $\mu = 26.5$ GPa [80], $\nu = 0.347$ [80] and $w = 5b$ [76] for Al-based solid solutions, with $a_0 = 4.049$ Å for pure Al and $a = 4.1125$ Å for the present metastable Al in a supersaturated solid solution based on the XRD analysis.

Fig. 5 shows a comparison of yield strengths between an average of 1.24 GPa converted from the measured Vickers microhardness by recalculating as load divided by the projected area instead of surface area of the indented location as well as 1.3–1.5 GPa measured by nanoindentation for the metastable Al as shown by the horizontal dashed line and the horizontal hatched bar, respectively, together with
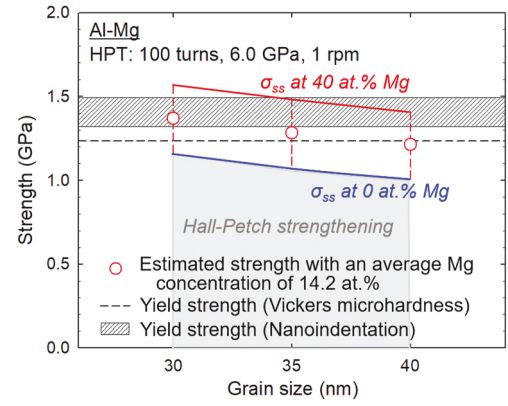


Fig. 5. Comparison of yield strength between the yield strength of 1.24 GPa converted from the measured Vickers microhardness value as well as 1.3–1.5 GPa measured by nanoindentation and the estimated hardness from a combination of Hall-Petch strengthening and solid solution strengthening with grain sizes of 30–40 nm for the nanostructured metastable Al in a supersaturated solid solution.

the computed strength by applying eqs (2)–(4) with an anticipated range of grain sizes of ~30–40 nm for the nanostructured metastable Al in a supersaturated solid solution. In practice, the estimated yield strength is shown from a minimum solution strengthening with $X_{Mg} = 0$ at.% as a blue line to a maximum with $X_{Mg} = 40$ at.% as a red line with a weighted average Mg concentration of 14.2 at.% above the calculated strength by Hall-Petch strengthening which is shown in gray.

It is readily apparent that there is excellent agreement between the estimated yield strength for the nanostructured metastable Al having an average Mg concentration of 14.2 at.% and the experimentally measured strengths by Vickers microhardness measurements and nanoindentation that involve some scatters attributed in the indentation size effect demonstrating an increase in hardness with decreasing depth of penetration [81]. Nevertheless, it is important to note that the mean Mg concentration in Al is estimated to contribute >200 MPa to the total strength. Although there is a significant contribution from the grain refinement strengthening, it is clear that a supersaturation of Mg in the Al matrix is an essential requirement for achieving such high strength in the metastable Al in the supersaturated solid solution condition. It should be noted that high hardness at the disk edge of the mechanically-bonded Al–Mg alloy after 10 turns was demonstrated by the highest contribution of grain refinement with concurrent small contributions of solid-solution strengthening and the precipitation strengthening attributed to the presence of nanostructured $Al_2Mg_3$ and $Al_{12}Mg_{17}$ intermetallic compounds [25]. Therefore, the structural transformation provides significant contributions to the total hardness value of the Al–Mg alloy synthesized by HPT. Moreover, it is anticipated that there will be a softening of the metastable Al with further aging leading to a decomposition of the Al–Mg intermetallic phases [62] and further investigations will be needed to fully explore these possibilities.

### 4.2. Structural stability and microstrains

Several reports are currently available for estimating the crystallite sizes and microstrain from analyses of X-ray diffraction data on bulk nanostructured materials processed by SPD techniques [66,82–86], nanomaterials synthesized by powder metallurgy and a mechanical alloying approach [72,87–92] and nanoparticles and thin films [93–96]. These results are summarized in Fig. 6. The dashed line shows the typical trend for the relationship between microstrain and crystallite size for these nanostructured materials and nanomaterials and it is readily apparent that a high microstrain may be attained only in materials having very small crystallite sizes.

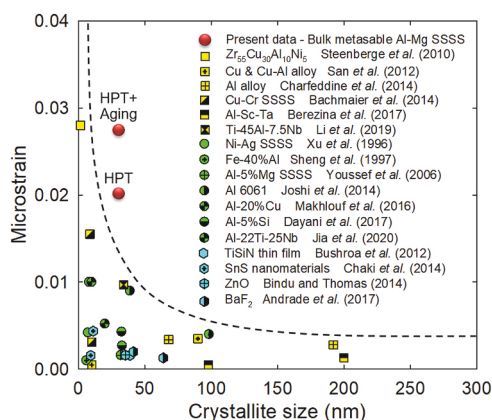The present experimental data on the metastable Al immediately

**Fig. 6.** A plot of the microstrain versus crystallite size measured by XRD analysis on bulk nanostructured materials processed by SPD [66,82–86], nanomaterials synthesized by powder metallurgy and a mechanical alloying approach [72,87–92] and nanoparticles and thin films [93–96].

after HPT and after natural aging are also displayed in Fig. 6 by applying the microstrains estimated in Fig. 4 with a grain size of 35–40 nm as crystallite sizes for the HPT-processed nanostructured metastable Al. At these levels of the crystallite sizes, a very high microstrain is visualized in the metastable Al and this microstrain is even larger after natural aging. As noted earlier, this is attributed to the compositional line broadening caused by a heterogeneous distribution of Mg supersaturation in the Al matrix during the aging process. Also, there may be some stressed-induced broadening which is superimposed but it cannot be separated from the dominant chemical strain in this study. Although some materials show supersaturated solid solution phases [72,85,87], the total volumes of supersaturated solutes are not comparable to the present experiments involving supersaturated Mg solutes with a maximum solubility of ~38.4 at.% in Al as shown by the large peak shifting in the X-ray diffraction analyses. Very limited information is available to date on an Al–Mg system but nevertheless the present HPT-induced bulk metastable Al–Mg after 100 turns and natural aging appears to contain a significantly higher microstrain while maintaining a single-phase state.

## 5. Summary and conclusions

1. Bulk nanostructured metastable Al solid solution alloys with supersaturation of Mg demonstrate excellent mechanical responses including strength and plasticity, and with structural stability after 60 days of natural aging.

2. The excellent plasticity was recorded by estimating the strain rate sensitivity of $m \approx 0.036$ for the bulk metastable Al–Mg after 100 turns. The extreme strength of ~1.5 GPa for the metastable alloy is satisfactorily explained through a summation of strengthening by grain refinement and solid solution strengthening.

3. Unique line broadening with a plateau shape was observed in the HPT-induced metastable Al alloy followed by natural aging, revealing a heterogeneous distribution of supersaturated Mg solutes within the disk surface and in the disk height direction.

4. Significant XRD peak shifting from pure Al due to exceptional microstrains of ~0.0202 and ~0.0274 were observed without any nucleation of a second phase for the metastable Al after HPT and after natural aging, respectively.

## Data availability

The data that support the findings of this study are available from the corresponding author on reasonable request.

## CRediT authorship contribution statement

**Jae-Kyung Han:** carried out all of the technical details, and performed the numerical calculations for the suggested experiment. **Klaus-Dieter Liss:** Formal analysis, Data curation, analyzed the XRD data and derived the models. provided critical feedback on the manuscript. **Terence G. Langdon:** provided critical feedback on the manuscript. **Jae-il Jang:** carried out the nanoindentation experiments. **Megumi Kawasaki:** Project administration, Writing - original draft, designed, directed the project, and wrote the manuscript.

## Declaration of competing interest

The authors declare that they have no known competing financial interests or personal relationships that could have appeared to influence the work reported in this paper.

## Acknowledgements

## References

[1] R.Z. Valiev, Y. Estrin, Z. Horita, T.G. Langdon, M.J. Zehetbauer, Y.T. Zhu, Producing bulk ultrafine-grained materials by severe plastic deformation, JOM 58 (4) (2006) 33–39, https://doi.org/10.1007/s11837-006-0213-7.

[2] R.Z. Valiev, Y. Estrin, Z. Horita, T.G. Langdon, M.J. Zehetbauer, Y.T. Zhu, Producing bulk ultrafine-grained materials by severe plastic deformation: ten years later, JOM 68 (2016) 1216–1226, https://doi.org/10.1007/s11837-016-1820-6.

[3] R.Z. Valiev, Y. Estrin, Z. Horita, T.G. Langdon, M.J. Zehetbauer, Y.T. Zhu, Fundamentals of superior properties in bulk nanoSPD materials, Mater. Res. Lett. 4 (2016) 1–21, https://doi.org/10.1080/21663831.2015.1060543.

[4] A.P. Zhilyaev, T.G. Langdon, Using high-pressure torsion for metal processing: fundamentals and applications, Prog. Mater. Sci. 53 (2008) 893–979, https://doi.org/10.1016/j.pmatsci.2008.03.002.

[5] T.G. Langdon, Twenty-five years of ultrafine-grained materials: achieving exceptional properties through grain refinement, Acta Mater. 61 (2013) 7035–7059, https://doi.org/10.1016/j.actamat.2013.08.018.

[6] A.P. Zhilyaev, A.A. Gimazov, G.I. Raab, T.G. Langdon, Using high-pressure torsion for the cold-consolidation of copper chips produced by machining, Mater. Sci. Eng., A 486 (2008) 123–126, https://doi.org/10.1016/j.msea.2007.08.070.

[7] K. Edalati, Y. Yokoyama, Z. Horita, High-pressure torsion of machining chips and bulk discs of amorphous $Zr_{50}Cu_{30}Al_{10}Ni_{10}$, Mater. Trans. 51 (2010) 23–26, https://doi.org/10.2320/matertrans.MB200914.

[8] M.M. Castro, P.H.R. Pereira, A. Isaac, R.B. Figueiredo, T.G. Langdon, Development of a magnesium-alumina composite through cold consolidation of machining chips by high-pressure torsion, J. Alloys Compd. 780 (2019) 422–427, https://doi.org/10.1016/j.jallcom.2018.11.357.

[9] A.V. Korznikov, I.M. Safarov, D.V. Laptionok, R.Z. Valiev, Structure and properties of superfine-grained iron compacted out of ultradisperse powder, Acta Metall. Mater. 39 (1991) 3193–3197, https://doi.org/10.1016/0956-7151(91)90054-5.

[10] V.V. Stolyarov, Y.T. Zhu, T.C. Lowe, R.K. Islamgaliev, R.Z. Valiev, Processing nanocrystalline Ti and its nanocomposites from micrometer-sized Ti powder using high pressure torsion, Mater. Sci. Eng., A 282 (2000) 78–85, https://doi.org/10.1016/S0921-5093(99)00764-9.

[11] K. Edalati, Z. Horita, H. Fujiwara, K. Ameyama, Cold consolidation of ball-milled titanium powders using high-pressure torsion, Metall. Mater. Trans. A 41A (2010) 3308–3317, https://doi.org/10.1007/s11661-010-0400-6.

[12] J.M. Cubero-Sesin, Z. Horita, Powder consolidation of Al–10 wt% Fe alloy by high-pressure torsion, Mater. Sci. Eng., A 558 (2012) 462–471, https://doi.org/10.1016/j.msea.2012.08.029.

[13] Y. Zhang, S. Sabbaghianrad, H. Yang, T.D. Topping, T.G. Langdon, E.J. Lavernia, J.M. Schoenung, S.R. Nutt, Two-step SPD processing of a trimodal Al-based nanocomposite, Metall. Mater. Trans. 46A (2015) 5877–5886, https://doi.org/10.1007/s11661-015-3151-6.

[14] A.P. Zhilyaev, G. Ringot, Y. Huang, J.M. Cabrera, T.G. Langdon, Mechanical behavior and microstructure properties of titanium powder consolidated by high-pressure torsion, Mater. Sci. Eng., A 688 (2017) 498–504, https://doi.org/10.1016/j.msea.2017.02.032.

[15] Y. Huang, P. Bazarnik, D. Wan, D. Luo, P.H.R. Pereira, M. Lewandowska, J. Yao, B.E. Hayden, T.G. Langdon, The fabrication of graphene-reinforced Al-based

nanocomposites using high-pressure torsion, Acta Mater. 164 (2019) 499–511, https://doi.org/10.1016/j.actamat.2018.10.060.

[16] X. Sauvage, P. Jessner, F. Vurpillot, R. Pippan, Nanostructure and properties of a Cu–Cr composite processed by severe plastic deformation, Scripta Mater. 58 (2008) 1125–1128, https://doi.org/10.1016/j.scriptamat.2008.02.010.

[17] A. Bachmaier, M. Kerber, D. Setman, R. Pippan, The formation of supersaturated solid solutions in Fe–Cu alloys deformed by high-pressure torsion, Acta Mater. 60 (2012) 860–871, https://doi.org/10.1016/j.actamat.2011.10.044.

[18] K. Oh-ishi, K. Edalati, H.S. Kim, K. Hono, Z. Horita, High-pressure torsion for enhanced atomic diffusion and promoting solid-state reactions in the aluminum–copper system, Acta Mater. 61 (2013) 3482–3489, https://doi.org/10.1016/j.actamat.2013.02.042.

[19] O. Bouaziz, H.S. Kim, Y. Estrin, Architecturing of metal-based composites with concurrent nanostructuring: a new paradigm of materials design, Adv. Eng. Mater. 15 (2013) 336–340, https://doi.org/10.1002/adem.201200261.

[20] M. Pouryazdan, B.J.P. Kaus, A. Rack, A. Ershov, H. Hahn, Mixing instabilities during shearing of metals, Nat. Commun. 8 (2017) 1611, https://doi.org/10.1038/s41467-017-01879-5.

[21] J.-K. Han, D.K. Han, G.Y. Liang, J.-i. Jang, T.G. Langdon, M. Kawasaki, Direct bonding of aluminum-copper metals through high-pressure torsion processing, Adv. Eng. Mater. 20 (2018) 1800642, https://doi.org/10.1002/adem.201800642.

[22] R. Kulagin, Y. Beygelzimer, Yu. Ivanisenko, A. Mazilkin, B. Straumal, H. Hahn, Instabilities of interfaces between dissimilar metals induced by high pressure torsion, Mater. Lett. 222 (2018) 172–175, https://doi.org/10.1016/j.matlet.2018.03.200.

[23] V.N. Danilenko, S.N. Sergeev, J.A. Baimova, G.F. Korznikova, K.S. Nazarov, R. Kh. Khisamov, A.M. Glezer, R.R. Mulyukov, An approach for fabrication of Al-Cu composite by high pressure torsion, Mater. Lett. 236 (2019) 51–55, https://doi.org/10.1016/j.matlet.2018.09.158.

[24] X. Qiao, X. Li, X. Zhang, Y. Chen, M. Zheng, I.S. Golovin, N. Gao, M.J. Starink, Intermetallics formed at interface of ultrafine grained Al/Mg bi-layered disks processed by high pressure torsion at room temperature, Mater. Lett. 181 (2016) 187–190, https://doi.org/10.1016/j.matlet.2016.06.035.

[25] B. Ahn, A.P. Zhilyaev, H.-J. Lee, M. Kawasaki, T.G. Langdon, Rapid synthesis of an extra hard metal matrix nanocomposite at ambient temperature, Mater. Sci. Eng., A 635 (2015) 109–117, https://doi.org/10.1016/j.msea.2015.03.042.

[26] M. Kawasaki, B. Ahn, H.-J. Lee, A.P. Zhilyaev, T.G. Langdon, Using high-pressure torsion to process an aluminum–magnesium nanocomposite through diffusion bonding, J. Mater. Res. 31 (2016) 88–99, https://doi.org/10.1557/jmr.2015.257.

[27] B. Ahn, H.-J. Lee, I.-C. Choi, M. Kawasaki, J.-i. Jang, T.G. Langdon, Micromechanical behavior of an exceptionally strong metal matrix nanocomposite processed by high-pressure torsion, Adv. Eng. Mater. 18 (2016) 1001–1008, https://doi.org/10.1002/adem.201500520.

[28] J.-K. Han, H.-J. Lee, J.-i. Jang, M. Kawasaki, T.G. Langdon, Micro-mechanical and tribological properties of aluminum-magnesium nanocomposites processed by high-pressure torsion, Mater. Sci. Eng., A 684 (2017) 318–327, https://doi.org/10.1016/j.msea.2016.12.067.

[29] M. Kawasaki, S.H. Jung, J.-M. Park, J. Lee, J.-i. Jang, J.-K. Han, Mechanical bonding of aluminum hybrid alloy systems through high-pressure torsion, Adv. Eng. Mater. 22 (2020) 1900483, https://doi.org/10.1002/adem.201900483.

[30] J.-K. Han, J.-M. Park, W. Ruan, K.T. Carpenter, A. Tabei, J.-i. Jang, M. Kawasaki, Size effect on microstructural evolution and micromechanical responses of mechanically bonded aluminum and magnesium by high-pressure torsion, Adv. Eng. Mater. (2019) 1900971, https://doi.org/10.1002/adem.201900971.

[31] M.M. Castro, S. Sabbaghianrad, P.H.R. Pereira, E.M. Mazzer, A. Isaac, T. G. Langdon, R.B. Figueiredo, A magnesium-aluminum composite produced by high-pressure torsion, J. Alloys Compd. 804 (2019) 421–426, https://doi.org/10.1016/j.jallcom.2019.07.007.

[32] J.-K. Han, K.-D. Liss, T.G. Langdon, M. Kawasaki, Synthesis of a bulk nanostructured metastable Al alloy with extreme supersaturation of Mg, Sci. Rep. 9 (2019) 17186, https://doi.org/10.1038/s41598-019-53614-3.

[33] M. Kawasaki, J.-K. Han, D.-H. Lee, J.-i. Jang, T.G. Langdon, Fabrication of nanocomposites through diffusion bonding under high-pressure torsion, J. Mater. Res. 33 (2018) 2700–2710, https://doi.org/10.1557/jmr.2018.205.

[34] J.-K. Han, T. Herndon, J.-i. Jang, T.G. Langdon, M. Kawasaki, Synthesis of hybrid nanocrystalline alloys by mechanical bonding through high-pressure torsion, Adv. Eng. Mater. 22 (2020) 1901289, https://doi.org/10.1002/adem.201901289.

[35] T. Miyazaki, D. Terada, Y. Miyajima, C. Suryanarayana, R. Murao, Y. Yokoyama, K. Sugiyama, M. Umemoto, Y. Todaka, N. Tsuji, Synthesis of non-equilibrium phases in immiscible metals mechanically mixed by high pressure torsion, J. Mater. Sci. 46 (2011) 4296–4301, https://doi.org/10.1007/s10853-010-5240-7.

[36] N. Ibrahim, M. Peterlechner, F. Emeis, M. Wegner, S.V. Divinski, G. Wilde, Mechanical alloying via high-pressure torsion of the immiscible $Cu_{50}Ta_{50}$ system, Mater. Sci. Eng., A 685 (2017) 19–30, https://doi.org/10.1016/j.msea.2016.12.106.

[37] T. Mousavi, J. Dai, P. Bazarnik, P.H.R. Pereira, Y. Huang, M. Lewandowska, T. G. Langdon, Fabrication and characterization of nanostructured immiscible Cu–Ta alloys processed by high-pressure torsion, J. Alloys Compd. 832 (2020) 155007, https://doi.org/10.1016/j.jallcom.2020.155007.

[38] Y. Qi, A. Kosinova, A.R. Kilmametov, B.B. Straumal, E. Rabkin, Plastic flow and microstructural instabilities during high-pressure torsion of Cu/ZnO composites, Mater. Char. 145 (2018) 389–401, https://doi.org/10.1016/j.matchar.2018.09.001.

[39] S.O. Rogachev, R.V. Sundeev, V.M. Khatkevich, Evolution of the structure and strength of steel/vanadium alloy/steel hybrid material during severe plastic

[40] deformation, Mater. Lett. 173 (2016) 123–126, https://doi.org/10.1016/j.matlet.2016.03.044.

[40] S.O. Rogachev, S.A. Nikulin, A.B. Rozhnov, V.M. Khatkevich, T.A. Nechaykina, M. V. Gorshenkov, R.V. Sundeev, Multilayer "steel/vanadium alloy/steel" hybrid material obtained by high-pressure torsion at different temperatures, Metall. Mater. Trans. A 48A (2017) 6091–6101, https://doi.org/10.1007/s11661-017-4342-0.

[41] S.O. Rogachev, R.V. Sundeev, N.Yu. Tabachkova, High pressure torsion-induced amorphous phase in a multilayer V-10Ti-5Cr/Zr-2.5Nb/V-10Ti-5Cr hybrid material, Mater. Lett. 234 (2019) 220–223, https://doi.org/10.1016/j.matlet.2018.09.112.

[42] D. Hernández-Escobar, Z.U. Rahman, H. Yilmazer, M. Kawasaki, C.J. Boehlert, Microstructural evolution and intermetallic formation in Zn-Mg hybrids processed by high-pressure torsion, Phil. Mag. 99 (2019) 557–584, https://doi.org/10.1080/14786435.2018.1546962.

[43] D. Hernández-Escobar, J. Marcus, J.-K. Han, R.R. Unocic, M. Kawasaki, C. J. Boehlert, Effect of post-deformation annealing on the microstructure and micro-mechanical behavior of Zn–Mg hybrids processed by high-pressure torsion, Mater. Sci. Eng., A 771 (2020) 138578, https://doi.org/10.1016/j.msea.2019.138578.

[44] D. Hernández-Escobar, R.R. Unocic, M. Kawasaki, C.J. Boehlert, High-pressure torsion processing of Zn–3Mg alloy and its hybrid counterpart: a comparative study, J. Alloys Compd. 831 (2020) 154891, https://doi.org/10.1016/j.jallcom.2020.154891.

[45] D. Luo, T. Huminiuc, Y. Huang, T. Polcar, T.G. Langdon, The fabrication of high strength Zr/Nb nanocomposites using high-pressure torsion, Mater. Sci. Eng., A 790 (2020) 139693, https://doi.org/10.1016/j.msea.2020.139693.

[46] D.A. Rigney, S. Karthikeyan, The evolution of tribomaterial during sliding: a brief introduction, Tribol. Lett. 39 (2010) 3–7, https://doi.org/10.1007/s11249-009-9498-3.

[47] W. Thomson, XLVI. Hydrokinetic solutions and observations, Philos. Mag. J. Sci. 42 (1871) 362–377, https://doi.org/10.1080/14786447108640585.

[48] H. von Helmholtz, XLIII. On discontinuous movements of fluids, Philos. Mag. J. Sci. 36 (1868) 337–346, https://doi.org/10.1080/14786446808640073.

[49] Y. Cao, M. Kawasaki, Y.B. Wang, S.N. Alhajeri, X.Z. Liao, W.L. Zheng, S.P. Ringer, Y.T. Zhu, T.G. Langdon, Unusual macroscopic shearing patterns observed in metals processed by high-pressure torsion, J. Mater. Sci. 45 (2010) 4545–4553, https://doi.org/10.1007/s10853-010-4485-5.

[50] R.H. Rangel, W.A. Sirignano, Nonlinear growth of Kelvin–Helmholtz instability: effect of surface tension and density ratio, Phys. Fluids 31 (1988) 1845–1855, https://doi.org/10.1063/1.866682.

[51] T.K.M. Nakamura, M. Fujimoto, Magnetic effects on the coalescence of Kelvin-Helmholtz vortices, Phys. Rev. Lett. 101 (2008) 165002, https://doi.org/10.1103/PhysRevLett.101.165002.

[52] I.P.D. De Silva, H.J.S. Fernando, F. Eaton, D. Hebert, Evolution of Kelvin-Helmholtz billows in nature and laboratory, Earth Planet Sci. Lett. 143 (1996) 217–231, https://doi.org/10.1016/0012-821X(96)00129-X.

[53] H. van Haren, L. Gostiaux, A deep-ocean Kelvin-Helmholtz billow train, Geophys. Res. Lett. 37 (2010) L03605, https://doi.org/10.1029/2009GL041890.

[54] Y. Beygelzimer, Vortices and mixing in metals during severe plastic deformation, Mater. Sci. Forum 683 (2011) 213–224, https://doi.org/10.4028/www.scientific.net/MSF.683.213.

[55] A. Gola, R. Schwaiger, P. Gumbsch, L. Pastewka, Vortices and mixing in metals during severe plastic deformation, Phys. Rev. Mater. 4 (2020), 013603, https://doi.org/10.1103/PhysRevMaterials.4.013603.

[56] C.L. Wang, Y.H. Lai, J.C. Huang, T.G. Nieh, Creep of nanocrystalline nickel: a direct comparison between uniaxial and nanoindentation creep, Scripta Mater. 62 (2010) 175–178, https://doi.org/10.1016/j.scriptamat.2009.10.021.

[57] I.-C. Choi, Y.-J. Kim, Y.M. Wang, U. Ramamurty, J.-i. Jang, Nanoindentation behavior of nanotwinned Cu: influence of indenter angle on hardness, strain rate sensitivity and activation volume, Acta Mater. 61 (2013) 7313–7323, https://doi.org/10.1016/j.actamat.2013.08.037.

[58] D. Tabor, Hardness of solids, Rev. Phys. Technol. 1 (1970) 145–179, https://doi.org/10.1088/0034-6683/1/3/I01.

[59] R.Z. Valiev, N.A. Enikeev, M.Yu. Murashkin, V.U. Kazykhanov, X. Sauvage, On the origin of the extremely high strength of ultrafine-grained Al alloys produced by severe plastic deformation, Scripta Mater. 63 (2010) 949–952, https://doi.org/10.1016/j.scriptamat.2010.07.014.

[60] I.-C. Choi, D.-H. Lee, B. Ahn, K. Durst, M. Kawasaki, T.G. Langdon, J.-i. Jang, Enhancement of strain-rate sensitivity and shear yield strength of a magnesium alloy processed by high-pressure torsion, Scripta Mater. 94 (2015) 44–47, https://doi.org/10.1016/j.scriptamat.2014.09.014.

[61] M. Kawasaki, B. Ahn, P. Kumar, J.-i. Jang, T.G. Langdon, Nano- and micro-mechanical properties of ultrafine-grained materials processed by severe plastic deformation techniques, Adv. Eng. Mater. 19 (2017) 1600578, https://doi.org/10.1002/adem.201600578.

[62] A.A. Mazilkin, B.B. Straumal, E. Rabkin, B. Baretzky, S. Enders, S.G. Protasova, O. A. Kogtenkova, R.Z. Valiev, Softening of nanostructured Al–Zn and Al–Mg alloys after severe plastic deformation, Acta Mater. 54 (2006) 3933–3939, https://doi.org/10.1016/j.actamat.2006.04.025.

[63] X. Sauvage, N. Enikeev, R. Valiev, Y. Nasedkina, M. Murashkin, Atomic-scale analysis of the segregation and precipitation mechanisms in a severely deformed Al–Mg alloy, Acta Mater. 72 (2014) 125–136, https://doi.org/10.1016/j.actamat.2014.03.033.

[64] J.H. Hubbell, S.M. Seltzer, Tables of X-ray Mass Attenuation Coefficients and Mass Energy-Absorption Coefficients from 1 keV to 20 MeV for Elements Z = 1 to 92 and 48 Additional Substances of Dosimetric Interest, NIST Standard Reference

Database 126, Version 1.4, National Institute of Standards and Technology, Gaithersburg, MD, 2004.

[65] WebElements™. http://www.webelements.com/.

[66] X. Li, R. Dippenaar, J.-K. Han, M. Kawasaki, K.-D. Liss, Phase transformation and structure evolution of a Ti-45Al-7.5Nb alloy processed by high-pressure torsion, J. Alloys Compd. 787 (2019) 1149–1157, https://doi.org/10.1016/j.jallcom.2019.02.174.

[67] R. Kulagin, Y. Beygelzimer, A. Bachmaier, R. Pippan, Y. Estrin, Benefits of pattern formation by severe plastic deformation, Appl. Mater. Today 15 (2019) 236–241, https://doi.org/10.1016/j.apmt.2019.02.007.

[68] Y. Cao, Y.B. Wang, S.N. Alhajeri, X.Z. Liao, W.L. Zheng, S.P. Ringer, T.G. Langdon, Y.T. Zhu, A visualization of shear strain in processing by high-pressure torsion, J. Mater. Sci. 45 (2010) 765–770, https://doi.org/10.1007/s10853-009-3998-2.

[69] Y. Cao, Y.B. Wang, R.B. Figueiredo, L. Chang, X.Z. Liao, M. Kawasaki, W.L. Zheng, S.P. Ringer, T.G. Langdon, Y.T. Zhu, Three-dimensional shear-strain patterns induced by high-pressure torsion and their impact on hardness evolution, Acta Mater. 59 (2011) 3903–3914, https://doi.org/10.1016/j.actamat.2011.03.015.

[70] R. Kulagin, Y. Beygelzimer, Y. Ivanisenko, A. Mazilkin, H. Hahn, High pressure torsion: from laminar flow to turbulence, IOP Conf. Ser. Mater. Sci. Eng. 194 (2017), https://doi.org/10.1088/1757-899X/194/1/012045, 012045.

[71] W. Jiang, H. Zhou, Y. Cao, J. Nie, Y. Li, Y. Zhao, M. Kawasaki, T.G. Langdon, Y. Zhu, On the heterogeneity of local shear strain induced by high-pressure torsion, Adv. Eng. Mater. 22 (2020) 1900477, https://doi.org/10.1002/adem.201900477.

[72] K.M. Youssef, R.O. Scattergood, K.L. Murty, C.C. Koch, Nanocrystalline Al–Mg alloy with ultrahigh strength and good ductility, Scripta Mater. 54 (2006) 251–256, https://doi.org/10.1016/j.scriptamat.2005.09.028.

[73] D. Zhao, O.M. Løvvik, K. Marthinsen, Y. Li, Impurity effect of Mg on the generalized planar fault energy of Al, J. Mater. Sci. 51 (2016) 6552–6568, https://doi.org/10.1007/s10853-016-9834-6.

[74] E.O. Hall, The deformation and ageing of mild steel: II characteristics of the Lüders deformation, Proc. Phys. Soc. B 64 (1951) 742–747, https://doi.org/10.1088/0370-1301/64/9/302.

[75] N.J. Petch, The cleavage strength of polycrystals, J. Iron Steel Inst. 174 (1953) 25–28.

[76] T. Uesugi, K. Higashi, First-principle studies on lattice constants and local lattice distortions in solid solution aluminum alloys, Comput. Mater. Sci. 67 (2013) 1–10, https://doi.org/10.1016/j.commatsci.2012.08.037.

[77] Z.C. Cordero, B.E. Knight, C.A. Schuh, Six decades of the Hall-Petch effect - a survey of grain-size strengthening studies on pure metals, Int. Mater. Rev. 61 (2016) 495–512, https://doi.org/10.1080/09506608.2016.1191808.

[78] G.B. Burger, A.K. Gupta, P.W. Jeffrey, D.J. Lloyd, Microstructural control of aluminum sheet used in automotive applications, Mater. Char. 35 (1995) 23–39, https://doi.org/10.1016/1044-5803(95)00065-8.

[79] R.E. Stoller, S.J. Zinkle, On the relationship between uniaxial yield strength and resolved shear stress in polycrystalline materials, J. Nucl. Mater. 283–287 (2000) 349–352, https://doi.org/10.1016/S0022-3115(00)00378-0.

[80] J.P. Hirth, J. Lothe, Theory of Dislocations, second ed., Wiley, New York, 1982, p. 839.

[81] W.D. Nix, H. Gao, Indentation size effects in crystalline materials: a law for strain gradient plasticity, J. Mech. Phys. Solid. 46 (1998) 411–425, https://doi.org/10.1016/S0022-5096(97)00086-0.

[82] N.V. Steenberge, S. Hóbor, S. Suriñach, A.P. Zhilyaev, F. Houdellier, F. Mompiou, M.D. Baró, Á. Révész, J. Sort, Effects of severe plastic deformation on the structure and thermo-mechanical properties of $Zr_{55}Cu_{30}Al_{10}Ni_5$ bulk metallic glass, J. Alloys Compd. 500 (2010) 61–67, https://doi.org/10.1016/j.jallcom.2010.03.195.

[83] X.Y. San, X.G. Liang, L.P. Cheng, L. Shen, X.K. Zhu, Effect of stacking fault energy on mechanical properties of ultrafine-grain Cu and Cu–Al alloy processed by cold-rolling, Trans. Nonferrous Metals Soc. China 22 (2012) 819–824, https://doi.org/10.1016/S1003-6326(11)61250-8.

[84] S. Charfeddine, K. Zehani, L. Besais, A. Korchef, Grain refinement and lattice imperfections in commercial aluminum alloy processed by severe plastic deformation, IOP Conf. Ser. Mater. Sci. Eng. 62 (2014), https://doi.org/10.1088/1757-899X/62/1/012003, 012003.

[85] A. Bachmaier, G.B. Rathmayr, M. Bartosik, D. Apel, Z. Zhang, R. Pippan, New insights on the formation of supersaturated solid solutions in the Cu–Cr system deformed by high-pressure torsion, Acta Mater. 69 (2014) 301–313, https://doi.org/10.1016/j.actamat.2014.02.003.

[86] A. Berezina, T. Monastyrska, O. Davydenko, O. Molebny, S. Polishchuk, Effect of severe plastic deformation on structure and properties of Al-Sc-Ta and Al-Sc-Ti alloys, Nanoscale Res. Lett. 12 (2017) 220, https://doi.org/10.1186/s11671-017-1995-y.

[87] J. Xu, U. Herr, T. Klassen, R.S. Averback, Formation of supersaturated solid solutions in the immiscible Ni–Ag system by mechanical alloying, J. Appl. Phys. 79 (1996) 3935–3945, https://doi.org/10.1063/1.361820.

[88] H.W. Sheng, Y.H. Zhao, Z.Q. Hu, K. Lu, Lattice instability in the solid-state amorphization of Fe(Al) solid solutions by mechanical alloying, Phys. Rev. B 56 (1997) 2302–2305, https://doi.org/10.1103/PhysRevB.56.2302.

[89] R.S. Joshi, S. Srivastava, H. Singh, Microstructural analysis of nanostructured aluminum alloy strips created from machining based deformation process, Procedia CIRP 14 (2014) 130–135, https://doi.org/10.1016/j.procir.2014.03.036.

[90] M.B. Makhlouf, T. Bachaga, J.J. Sunol, M. Dammak, M. Khitouni, Synthesis and characterization of nanocrystalline Al-20 at. % Cu powders produced by mechanical alloying, Metals 6 (7) (2016) 145, https://doi.org/10.3390/met6070145.

[91] D. Dayani, A. Shokuhfar, M.R. Vaezi, S.R.J. Rezaei, S. Hosseinpour, Structural and mechanical evaluation of a nanocrystalline Al–5 wt %Si alloy produced by mechanical alloying, Metals 7 (9) (2017) 332, https://doi.org/10.3390/met7090332.

[92] J. Jia, W. Sun, W. Peng, Z. Yang, Y. Xu, X.X. Zhong, W. Liu, J. Luo, Preparation of Ti-22Al-25Nb solid solution powders using mechanical alloying and solid solution mechanism analysis, Adv. Powder Technol. 31 (2020) 1963–1974, https://doi.org/10.1016/j.apt.2020.02.029.

[93] A.R. Bushroa, R.G. Rahbari, H.H. Masjuki, M.R. Muhamad, Approximation of crystallite size and microstrain via XRD line broadening analysis in TiSiN thin films, Vacuum 86 (2012) 1107–1112, https://doi.org/10.1016/j.vacuum.2011.10.011.

[94] S.H. Chaki, M.D. Chaudhary, M.P. Deshpande, Synthesis and characterization of different morphological SnS nanomaterials, Adv. Nat. Sci. Nanosci. Nanotechnol. 5 (2014), https://doi.org/10.1088/2043-6262/5/4/045010, 045010.

[95] P. Bindu, S. Thomas, Estimation of lattice strain in ZnO nanoparticles: X-ray peak profile analysis, J. Theor. Appl. Phys. 8 (2014) 123–134, https://doi.org/10.1007/s40094-014-0141-9.

[96] A.B. Andrade, N.S. Ferreira, M.E.G. Valerio, Particle size effects on structural and optical properties of $BaF_2$ nanoparticles, RSC Adv. 7 (2017) 26839–26848, https://doi.org/10.1039/C7RA01582H.